

A new method for detailed discharge and volume measurements of debris flows based on high-frequency 3D LiDAR point clouds; Illgraben, Switzerland

Raffaele Spielmann^{a,b,*}, Jordan Aaron^{a,b}

^a Chair for Engineering Geology, Geological Institute, Department of Earth Sciences, ETH Zürich, Sonneggstrasse 5, 8092 Zurich, Switzerland

^b Swiss Federal Institute for Forest, Snow and Landscape Research WSL, Zürcherstrasse 111, 8903 Birmensdorf, Switzerland

ARTICLE INFO

Keywords:

Debris Flows
High-frequency LiDAR
Debris-flow Discharge
Debris-flow volume
Landslide monitoring

ABSTRACT

Debris flows are one of the most dangerous landslide types in mountainous regions. Their destructiveness is strongly controlled by their high peak discharge, which can be orders of magnitude larger than for floods. In order to reduce the associated hazards, detailed field measurements of natural debris flows are required to better constrain discharge and volume of these events. In this study, we used a high-frequency 3D LiDAR (light detection and ranging) scanner in combination with video cameras to measure key properties of a debris flow that occurred in the Illgraben catchment (Switzerland). Based on the LiDAR and video data, we directly measured i) front velocity ii) surge velocity iii) surface velocity and iv) cross-sectional area at sub-second intervals. We then estimated discharge and volume using these direct measurements and considering different channel bed geometry scenarios. We compared our results to estimates based on conventional methods and found that these more established methods substantially underestimate the (peak) discharge and volume for this event. Our results will be assessed in the future by analyzing more events, but our LiDAR-based method has the potential to provide much more detailed information on hazard-related debris-flow parameters, which will have important implications for understanding debris-flow processes and ultimately reducing their risk.

1. Introduction

Debris flows are very rapid to extremely rapid surging flows, composed of fine- and coarse-grained components, boulders, woody debris and water (Hungr et al., 2014). In mountainous regions, they represent one of the most hazardous landslide types (Badoux et al., 2009; Hürlimann et al., 2019) and lead to great destruction and many fatalities every year (e.g. Andres and Badoux, 2019; Dowling and Santi, 2014). Debris-flow intensity is strongly controlled by front velocity, peak discharge and event volume (Dowling and Santi, 2014; Jakob and Hungr, 2005). However, field scale measurements of these parameters are rare, despite being crucial for the design of mitigation measures, improved understanding of flow dynamics, the development, calibration and validation of debris-flow models, as well as the design of warning and alarm systems (Hürlimann et al., 2019; Jakob and Hungr, 2005). Here we present the results of a study that uses high-frequency 3D LiDAR (light detection and ranging) sensors, originally developed for autonomous vehicles, to measure these properties at high spatial and temporal

resolution. This is an emerging technology that has only started to be applied to natural hazard monitoring (Aaron et al., 2023; Spielmann, 2020).

Various researchers have measured the front and surface velocity of debris flows in different catchments worldwide using time-distance methods (Arattano et al., 2012; Comiti et al., 2014), video sequence analysis (Theule et al., 2018; Yan et al., 2016) or high-frequency radar measurements (Cui et al., 2018; Hübl et al., 2018). They found that the velocities in debris flows vary greatly, in particular between surge and inter-surge phases, with significant implications for estimating debris-flow discharge (Lapillonne et al., 2023).

Debris-flow discharge and volume have also been investigated by researchers at various catchments worldwide using a wide variety of methods. Many studies focused on peak discharge and analyzed debris flows at the event scale (e.g. Chen et al., 2007; Marchi et al., 2021; Rickenmann and Zimmermann, 1993). Other researchers focused on discharge estimates at the surge scale, as recently also suggested by Lapillonne et al. (2023), and assessed the discharge using surge

* Corresponding author at: ETH Zürich, Sonneggstrasse 5, 8092 Zurich, Switzerland.

E-mail address: raffaele.spielmann@erdw.ethz.ch (R. Spielmann).

velocities (e.g. Comiti et al., 2014; Li et al., 2017; Liu et al., 2009). A few other studies used instantaneous measurements of the (surface) velocity from video cameras (Cui et al., 2018) or 2D laser scanners (Jacquemart et al., 2017) to derive discharge. Furthermore, some studies did not derive the event volume from hydrographs, but directly derived volume from digital elevation models before and after an event (e.g. Coviello et al., 2020).

The most detailed methods used to measure debris-flow discharge, including those used in the present work, rely on surface measurements of the velocity and/or flow depth. These methods are limited by two factors, which are spatial and temporal changes in the shape of the vertical velocity profile, as well as erosion and deposition of material during flow. Recent studies have shown that the vertical velocity profile present in debris flows can vary between plug flow, and a profile that features internal shearing (Aaron et al., 2023; Nagl et al., 2020). This complicates the use of surface velocities when estimating discharge, as if

the velocity profile features internal shear than the depth-averaged velocity, and therefore discharge, will be overestimated (e.g. Cui et al., 2018). Also the second factor may have a substantial influence on discharge estimates as erosion with subsequent deposition can occur during an event (Berger et al., 2011a). Here we present a new method of estimating debris-flow discharge, which is able to explore the uncertainties related to these two factors.

While the studies detailed above have provided crucial insights into debris-flow velocity and discharge, persistent unknowns remain. In particular, the appropriateness of using average front and/or surge velocities to estimate discharge has not been rigorously verified. Recent advances in autonomous vehicles have provided new sensors and processing algorithms which can be leveraged to make measurements of surface velocity, flow depth and feature trajectories as well as to infer the vertical velocity profile of debris flows (Aaron et al., 2023). These recent advances have significant potential to overcome many of the

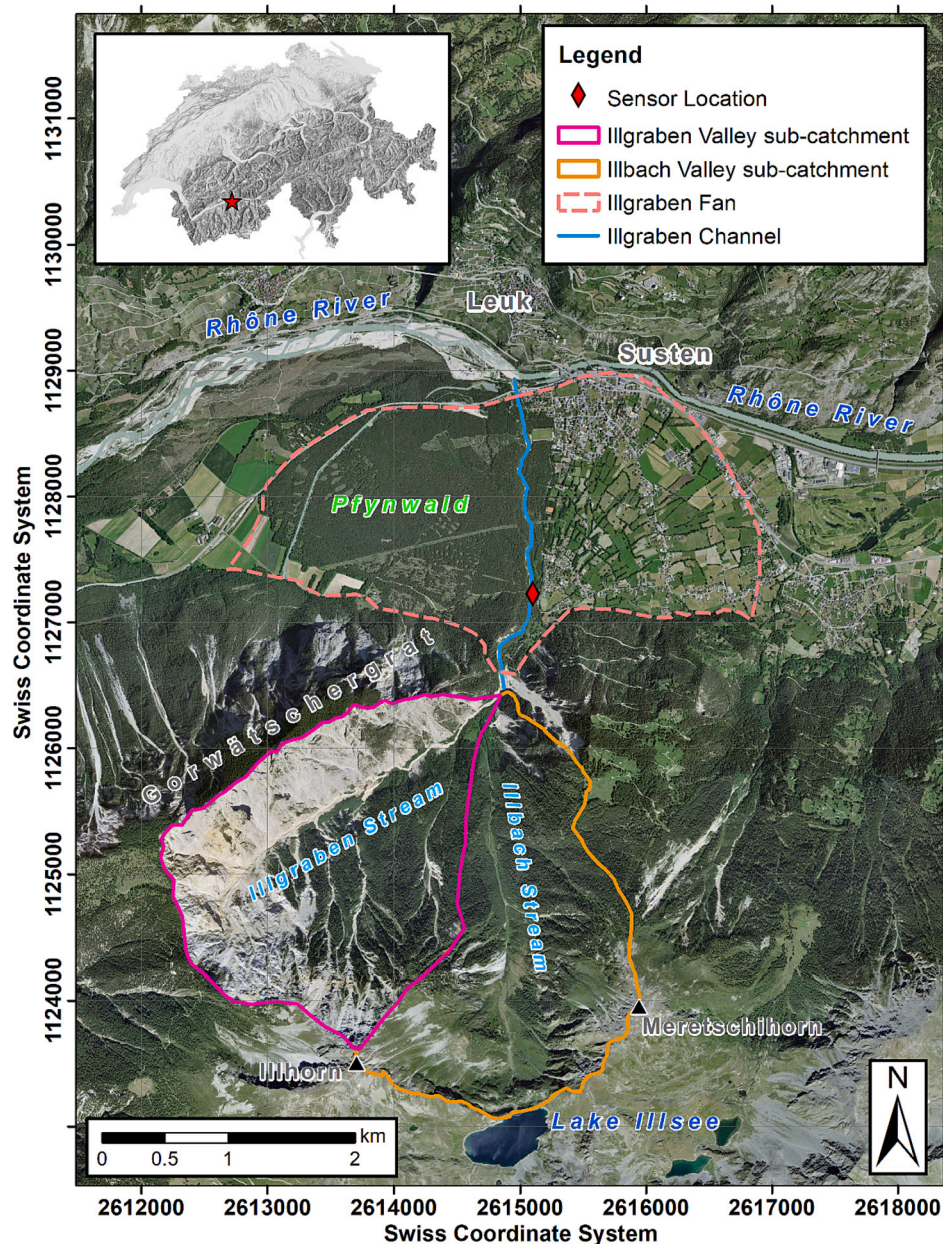


Fig. 1. Overview of the Illgraben catchment with sub-catchments and the fan. Debris flows initiate in the Illgraben valley sub-catchment. The LiDAR sensor location at the monitoring station “Gazoduc”, roughly 500 m downstream of the fan apex, is indicated in red (Orthophoto: Swiss Federal Office of Topography swisstopo). (For interpretation of the references to colour in this figure legend, the reader is referred to the web version of this article.)

limitations described above, and exploring this is the main subject of the present work.

In this study, we develop both manual and automated methods to track the debris-flow front over a channel segment and to derive its velocity. We further apply automated surface velocity and cross-sectional area measurement methods to multiple channel sections to derive the discharge over time and in space at three different, closely spaced sections upstream of a check dam. We account for potential changes in the shape of the channel bed by considering different channel geometry scenarios and include presumed changes in the vertical velocity profile in our instantaneous discharge derivation. We compare our results to discharge estimates based on the front and/or surge velocities, which represents a more conventional way to measure discharge, and find substantial discrepancies. Finally, we derive the volume of the debris flow using our LiDAR-based methodology and compare it to conventional approaches. This revealed that compared to the LiDAR-based methods proposed here, the conventional methods substantially underestimate the volume for the event analyzed in this work. The findings of the present study need to be assessed in the future by analyzing more events, but our LiDAR-based method has the potential to provide much more detailed and accurate information on hazard-related debris-flow parameters.

2. Study site, monitoring setup and data acquisition

2.1. Study site: Illgraben catchment

We installed our LiDAR sensor in the Illgraben catchment, which is located in the Canton of Valais in south-western Switzerland (Fig. 1). According to McArdell and Sartori (2021), the Illgraben is one of the most active debris-flow catchments in the Alps, with between two and ten debris flows occurring every year since the start of the systematic observation by the Swiss Federal Institute for Forest, Snow and Landscape Research WSL in June 2000 (Hürlimann et al., 2003). The Illgraben is located on the southern side of the Rhone River valley, near the village of Susten (Fig. 1). The torrent system extends from the Illhorn mountain (2716 m a.s.l.) to the Rhone River (ca. 610 m a.s.l.) and comprises a catchment (5.7 km², Illgraben valley sub-catchment, see Fig. 1) and a fan. The Illgraben Valley is located in highly fractured bedrock, which consists of Triassic dolomitic breccia, graywacke and marbles in the area northwest of the Illgraben stream and of quartzites in the southeastern part (McArdell and Sartori, 2021). Debris flows at the Illgraben typically occur following heavy rainfall from intense summer thunderstorms or weather fronts coming from the southwest (Graf et al., 2007; Hürlimann et al., 2019). This is typically between May and October, even though climate change scenarios project longer debris-flow seasons in the future (Hirschberg et al., 2021).

Several countermeasures, in particular check dams, were built in the 1970s to stabilize the catchment after a big debris-flow event in 1961 (Graf et al., 2007; Lichtenhahn, 1971; Missbauer, 1971). One of these check dams is commonly referred to as “Gazoduc” as it protects a gas pipeline, and is the location of our monitoring station with the LiDAR sensor (Fig. 1). The monitoring station “Gazoduc” is part of the WSL’s Illgraben Debris-Flow Monitoring Station, which also consists of other locations (Hürlimann et al., 2019). These stations are equipped with geophones to estimate front velocity and provide trigger signals for data loggers; ultrasonic, radar as well as laser stage sensors to determine flow depth; a large force plate to measure normal and shear forces and to determine (in combination with flow depth measurements) the density of a debris flow over time; and various video cameras (Badoux et al., 2009; Bennett et al., 2013; Berger et al., 2011b; Hürlimann et al., 2003; McArdell, 2016; McArdell et al., 2007). The mean slope angle in the channel segment immediately upstream of our LiDAR sensor and the check dam is 3.7° (cf. also Spielmann, 2022).

2.2. Monitoring setup and LiDAR scanner

The monitoring station “Gazoduc” is located next to a check dam and consists of a LiDAR scanner and a video camera, which are suspended in the middle of the channel ca. 6 m above the check dam, and a second camera on the channel bank (Fig. 2). The station is triggered by an upstream geophone.

In the present work, we collected data from a moving debris flow using an Ouster OS1-64 (Gen. 1) mid-range, multi-beam, high-resolution 3D LiDAR scanner (cf. also Spielmann, 2022, Spielmann, 2020). As indicated in Fig. 2, the LiDAR records at a frequency of 10 Hz and has a field of view of 33.2° and 64 scan lines distributed across this angle, leading to a vertical angular resolution of 0.53°. The scan lines were set to record 2048 points per rotation, which leads to a horizontal angular resolution of 0.18° (Ouster Inc, 2020). The LiDAR covers an area of ca. 40 m upstream and 60 m downstream of the check dam, but for the purpose of this work, we only analyzed the point cloud data in the channel segment upstream of the check dam (cf. Fig. SI 1). The manufacturer provides precision values for the sensor of ±1.1 cm for ranges of 1 m – 20 m, and ± 3 cm for ranges of 20 m to 50 m (Ouster Inc, 2020).

2.3. Acquired data: 19 September 2021, debris-flow event

On the 19 September 2021, the newly installed LiDAR scanner recorded a first debris-flow event (see also Aaron et al., 2023; Spielmann, 2022). The automated recording system was triggered at 08:40:25 (local time, UTC + 02:00) in the morning. The debris-flow front arrived at the check dam below the sensor at 08:42:29 (Fig. 3). For the purpose of this work, we will refer to the time of the event not in the local time format, but rather as *event time*, i.e. starting with the onset of the video and LiDAR recordings at 00:00 (mm:ss) event time, which corresponds to 08:40:25 local time.

The 19 Sept. event was the last debris flow of the 2021 debris-flow season. It occurred after several large and fast events in late June, July and August and smaller debris flows as well as hyper-concentrated flows in May and June (McArdell et al., 2023). A small but clearly recognizable pre-surge preceded the actual debris-flow front with its large boulders and woody debris. We defined the duration of the event as 30 min, which corresponds to the time when a transition to a (water) flood was observed.

A first analysis of this event has been performed by Aaron et al. (2023), and a few relevant details from that study are summarized here. Aaron et al. (2023) present two methods for automatically estimating surface velocity, one which is camera based, and the other which is based on hillshade projections of the LiDAR data. They further measure the velocity of a large number of boulders and pieces of woody debris. By combining these measurements, they show that the camera method measures the true surface velocity, whereas the hillshade method approaches the depth-averaged velocity. Further, they infer that the vertical velocity profile changes in this event, from a profile similar to plug-flow before 07:20, to a profile that features internal shearing after this time based on the ratio of 0.6–0.7 between the velocities of rolling boulders and woody debris. This increase in flow depth and velocity at 07:20 was referred to as the “velocity jump” and corresponds to the arrival of a second surge. The present work builds on these findings to explore the influence of a spatially and/or temporally variable vertical velocity profile on debris-flow discharge and volume.

3. Methods

We analyzed the point-cloud data to measure the front, surge and surface velocities as well as flow cross-sectional area, discharge and event volume. An overview of our workflow is shown in Fig. 4. As described in the following sections, we first pre-processed the point clouds, and then used these data to estimate key flow parameters. Further details about the methodology can also be found in Spielmann

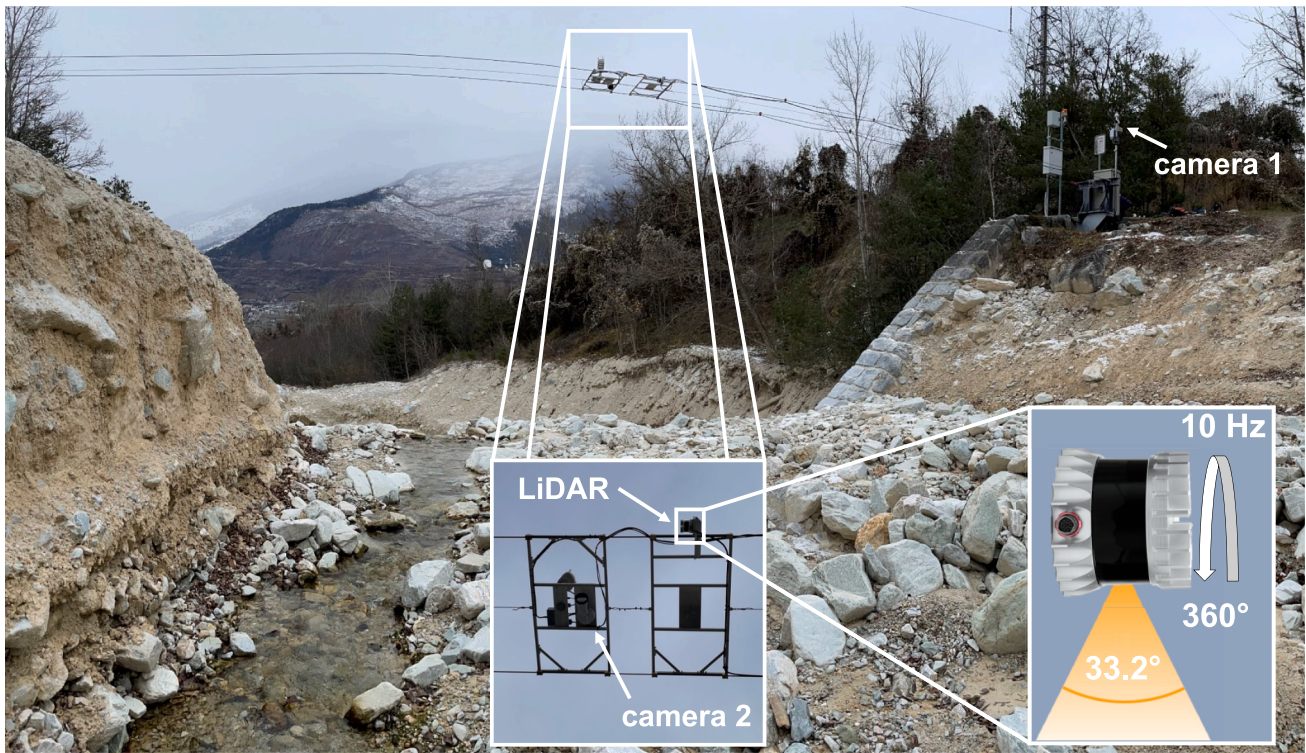


Fig. 2. Overview of the Illgraben debris-flow monitoring station “Gazoduc” (see also Fig. 1) with the LiDAR sensor suspended in the middle above a check dam and the two video cameras. The LiDAR sensor used here is an Ouster OS1-64 (Gen. 1) with a 33.2° field of view and a frame rate of 10 Hz.



Fig. 3. Video frames of the arrival of the flow front of the 19 Sept. 2021 debris-flow event in the Illgraben at the monitoring station “Gazoduc” (Fig. 1). The frames were recorded at 08:42:20 local time (corresponding to 01:55 event time; mm:ss) by a) camera1 and b) camera2 (see Fig. 2).

(2022).

3.1. Pre-Processing

For processing, it is convenient to use a *bed-parallel coordinate system*, as it simplifies many steps of the analysis. Further, the point clouds contain some artefacts, due to returns off raindrops and vegetation at the channel banks. We therefore pre-processed the point clouds prior to the main processing steps (Fig. 4). The first step of this pre-processing involved rotating the point clouds by the average channel slope angle upstream of the check dam (3.7°, see Sect. 2.1). The resulting bed-parallel coordinate system, which has one of the axes parallel to the channel slope, was the default coordinate system for this work and all the calculations and measurements were carried out using this frame of reference (see also Fig. SI 1).

Following the coordinate transformation, we cropped the original point clouds, which included reflections from objects outside of the

channel bed as well as from the section downstream of the check dam (which was not included in this analysis; cf. Sect. 2.2), to a 20 m × 50 m × 8 m sized box (along the x-, y- and z-axes, respectively; Fig. SI 1).

3.2. Front and surge velocity measurements

3.2.1. Manual front velocity measurement

The manual identification of the flow-front position was carried out in Matlabs’s *groundTruthLabeler*, using a method similar to the one described in Aaron et al. (2023) for features such as woody debris or boulders. We labelled the flow front in every fifth point cloud (i.e. at a frequency of 2 Hz). The labelling was performed manually by fitting a cuboid around the current flow front position (see also Fig. 7). We calculated the cumulative displacement of the front over time based on the sum of the Euclidean distances between subsequent (i.e. temporally 0.5 s apart) cuboid center positions. The velocity of the flow front could then be determined from the slope of the cumulative displacement over

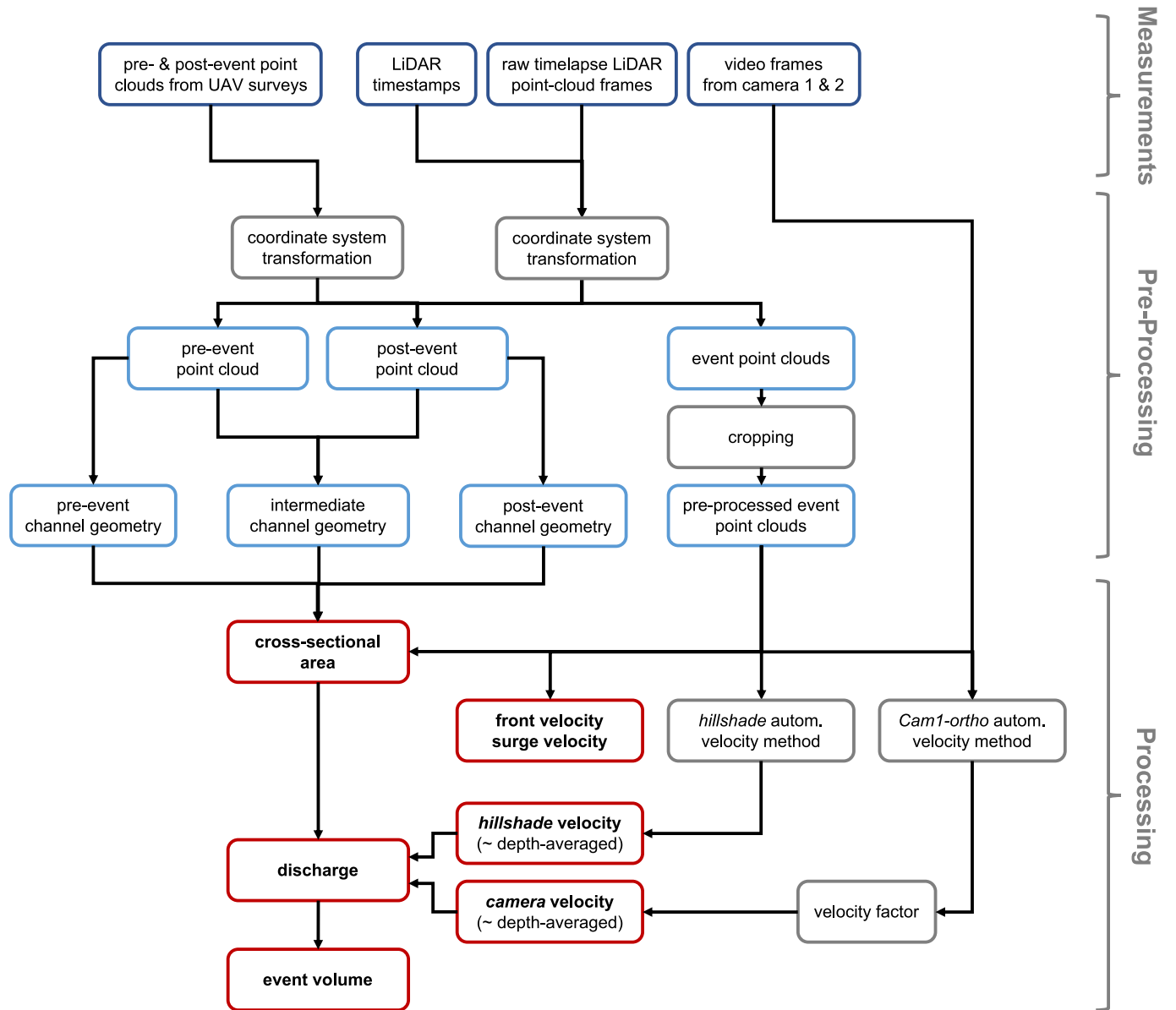


Fig. 4. Overview of the field measurements, pre-processing and processing workflow used in the present work to analyze the 3D LiDAR point-cloud data and to measure the relevant debris-flow parameters. For details, please refer to the following sections.

time.

3.2.2. Automated front velocity measurements

For the automated front velocity measurements, the point clouds recorded during the front arrival were compared to a reference point cloud, which had been recorded immediately prior to the arrival of the flow front. As the LiDAR scanner has a fixed spatial resolution of 64×2048 points per point cloud, a given point always measures the same location in a static scene. We therefore calculated the Euclidean distance between each point in the reference point cloud and its corresponding point in a point cloud recorded during the event. The points where this distance exceeded a geometrical threshold (0.4 m is used in the present work, cf. also Spielmann, 2022) were considered part of the moving flow.

Because some individual points not actually belonging to the front might exceed this threshold, we applied a filtering function (Matlab's *pcdenoise* function, cf. also Rusu et al., 2008) to the previously identified points. Consequently, for each timestep we obtained a filtered point cloud containing all points subject to motion, in which the location of

the flow front coincides with the points that have the smallest y-coordinates (i.e. are closest to the check dam, see also Fig. SI 1). In order to further avoid outliers, we isolated 250 points with the smallest y-coordinates and determined their mean position in every timestep, which corresponds to the position of the flow front. Finally, the distance between subsequent front positions was calculated as Euclidean distance, which allowed us to compute the cumulative displacement over time, and the velocity of the flow front could be derived by linear fitting to the corresponding time-displacement curve.

3.2.3. Surge velocity measurement

Even though we have much more detailed velocity measurements based on two different automated methods, we measured the velocity of a second surge manually as this is a requirement for the surge scale discharge methodology (Lapillonne et al., 2023), which we used as a comparison. We measured the velocity of the second surge by tracking an object at the head of the surge, i.e. a piece of woody debris, which could be easily identified and tracked similar to the flow front methodology.

3.3. Surface velocity measurement

We applied two methods to automatically derive the surface velocity of the moving flow (see also Aaron et al., 2023) in order to obtain two semi-independent measurements of this quantity. We used both methods to derive the surface velocity throughout the investigated channel segment, but evaluated them only at three channel sections (i.e. $y = 5$ m, $y = 10$ m, $y = 15$ m; see Fig. 5) to facilitate the analysis and as the measurements are most reliable at these distances (see below and Fig. SI 2). The first method is based on hillshade-projections from LiDAR point clouds and will thus be called the *hillshade* method. This method has already been described in Aaron et al. (2023), and involves creating hillshade images of each frame of the point clouds, and using these as input into a particle image velocimetry (PIV) algorithm to derive velocities (Thielicke and Sonntag, 2021). It is important to note that the LiDAR sensor does not cover the full channel width at channel sections close to the sensor (i.e. $y = 5$ m and $y = 10$ m; due to its limited field of view, cf. Fig. 5). Nonetheless, surface velocities can be measured within this field of view using the hillshade method and over the full channel width using the second method, as described below.

The second method is based on fusing the LiDAR and video camera footage and will be referred to as *camera1-ortho* (see also Fig. SI 3). The overall approach of the camera1-ortho method is to orthorectify the video imagery using the point-cloud data. For this, the point-cloud data was linearly interpolated to a 5 cm spacing. It was further extrapolated using the nearest neighbor method and clipped using the pre-event topography from photogrammetric unmanned aerial vehicle (UAV) flights (de Haas et al., 2022). This results in a point cloud that spans the entire channel, including the banks. Next, the point clouds were colored based on the projected video data (Aaron et al., 2023) to create orthophotos with a 5-cm resolution. These orthophotos were then input into PIVLab (Thielicke and Sonntag, 2021), a PIV software that is used to

derive a dense vector field of pixel displacements between subsequent images. We then re-project the 2D orthophoto displacements onto the corresponding point clouds to derive the z-component of displacement.

For both methods, following the derivation of the 3D velocities, we filter the velocities to exclude outliers (using limits of $-0.2 \text{ m/s} \leq v_x \leq 0.2 \text{ m/s}$ and $-4 \text{ m/s} \leq v_y \leq -1 \text{ m/s}$ for the velocity components along the x- and y-axes, respectively), smoothed the timeseries using a 30 s moving median and downsampled it to 1 s. We selected these values in order to exclude low velocity values / noise in the velocity vector field, which results from the PIV algorithm used. Nonetheless, we performed a sensitivity analysis with other filtering values, which is shown in the Supplementary Information (Fig. SI 7). Both methods have been validated by comparisons to manual measurements of features visible at the flow surface (Fig. SI 2). This validation revealed that the automated surface velocity measurements are only reliable for sections $y = 5$ m, $y = 10$ m and $y = 15$ m. Therefore, the other channel sections were not considered for velocity and, thus, discharge analysis (cf. also Spielmann, 2022).

For each of these three analyzed channel sections, we derived the average surface velocity across the channel section over the entire event based on the 3D surface velocity vector field from both automated methods. For each method, we calculated the mean of all velocity vectors across a given channel section, which provides us a (spatial) average cross-sectional velocity for each section and time. We then derived the magnitude of these 3D vectors to get the mean velocity at a given channel section over time and for later use in estimating discharge.

3.4. Cross-sectional area

We processed the LiDAR data to estimate the cross-sectional area of multiple, closely-spaced sections (Fig. 5). This required us to specify both 1) the surface of the flow and 2) the instantaneous geometry of the

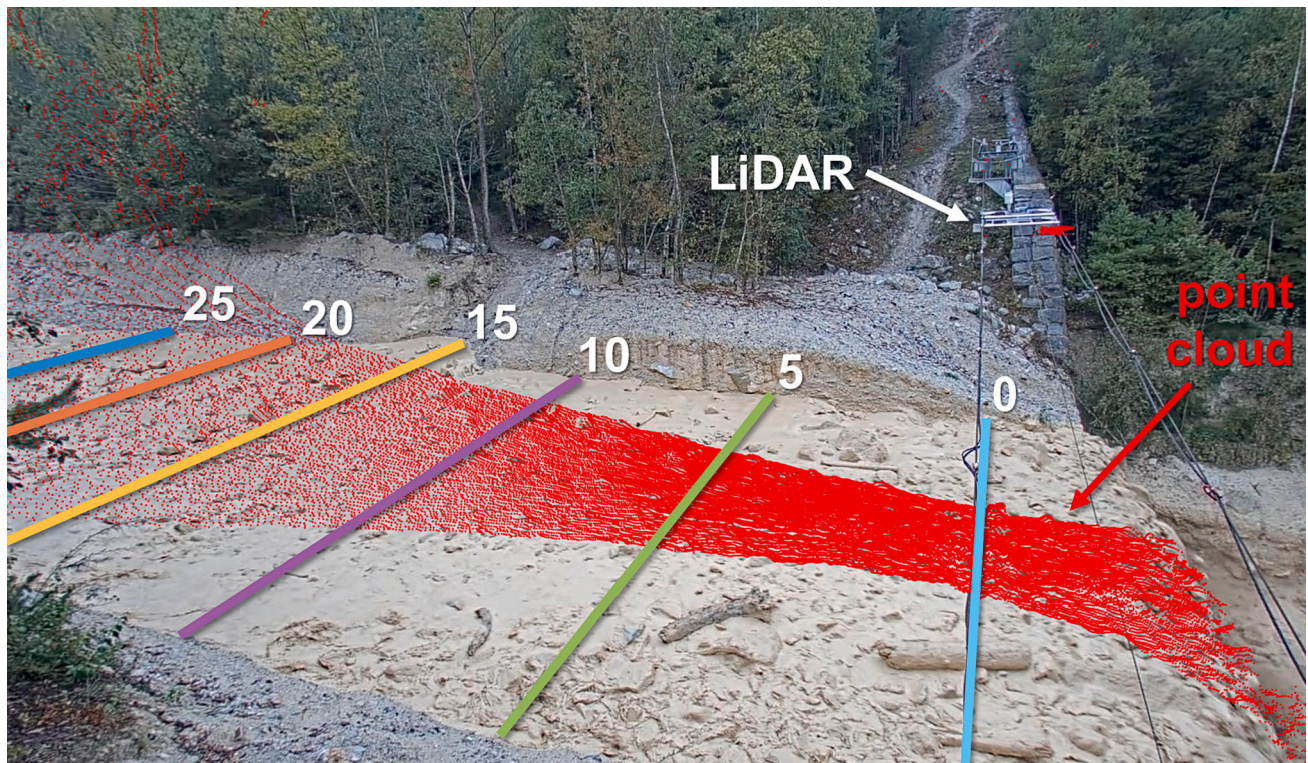


Fig. 5. Investigated channel segment with the six channel sections (numbers indicate upstream of sensor distance y in meters), where we measured the cross-sectional area (see also Fig. SI 6). The red dots indicate a point cloud recorded by the LiDAR scanner shortly after the front arrival (at 02:20) and were projected on a camera image (from camera1, see Fig. 2). The surface velocities were measured only at channel sections $y = 5$ m, $y = 10$ m and $y = 15$ m, as described above (see also Fig. SI 2).

channel bed. The LiDAR directly measures the surface of the flow, so item 1 could be directly derived by isolating the points in the point clouds at a given section and interpolating them (Fig. 6b). In order to exclude the channel banks, we automatically defined a flow-depth-based threshold (z -Threshold, based on the mean elevation of the flow surface in the middle of the channel, Fig. 6c) to exclude all the points in the point clouds of a given channel section which do not correspond to the moving debris flow. However, the LiDAR field of view is limited for the sections with y -coordinates <15 m (Fig. 5). To account for this, we extrapolated the flow surface from the channel middle to the banks, as the flow surface was largely horizontal in this event (see Fig. 6b).

The instantaneous geometry for the channel bed (item 2) was more complicated to derive, as the LiDAR only records the flow surface, and the height of the bed changes throughout the event due to erosion and/or deposition (e.g. Berger et al., 2011a). We accounted for this by defining three different *channel geometry scenarios* for each of the six channel sections (Fig. 6a, Fig. SI 4 and Fig. SI 5, as well as Jacquemart et al., 2017). These scenarios were based on point clouds recorded before (*pre-event channel geometry*) and after (*post-event channel geometry*) the 19 Sept. 2021 event. The third scenario, which we called *intermediate channel geometry*, was based on an interpreted combination of the pre- and post-event scans (Fig. SI 4 and Fig. SI 5). We derived the geometry for these scenarios either by using pre- and post-event LiDAR scans (for sections $y = 20$ m and $y = 25$ m), or digital terrain models (DTMs) from UAV flights (de Haas et al., 2022), for locations where the

LiDAR field of view is limited (for sections $y = 0$ m, $y = 5$ m, $y = 10$ m and $y = 15$ m, Fig. 5).

Finally, we combined the points representing the debris-flow surface at each channel section with each of the three corresponding channel base sections to obtain 2D sections through the debris flow and to measure the cross-sectional area. We used Matlab's *alphaShape* function, which creates a bounding area that envelops a set of 2D points and provides the area of a fitted shape, to measure this cross-sectional area (Fig. 6c).

3.5. Discharge

We used three different approaches to estimate the discharge of the 19 Sept. 2021 event. First, we present our newly developed LiDAR-based method, which uses instantaneous measurements of the velocity and cross-sectional area. Next, we describe how we implemented more established methods, and compare the results to our new method. These conventional methods are commonly used in instrumented catchments around the world (e.g. Hürlimann et al., 2019; Lapillonne et al., 2023). For each analyzed channel section, we obtained three discharge hydrographs, corresponding to the different channel bed geometry scenarios described above.

3.5.1. LiDAR-based discharge derivation

Discharge was estimated based on the surface velocity and the cross-

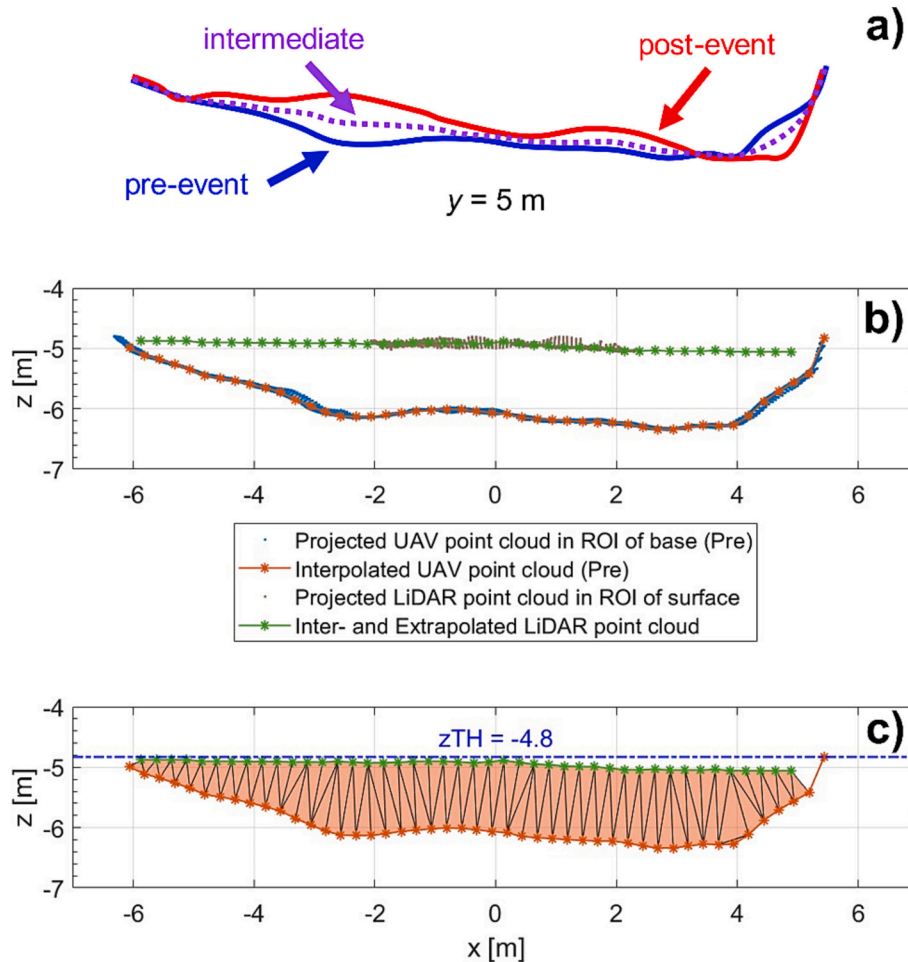


Fig. 6. a) Example of a channel section 5 m upstream of the LiDAR sensor with the three basal channel geometry scenarios (see Fig. SI 4 and Fig. SI 5 for details). b) Illustration of the interpolation of the channel base (pre-event from UAV) and interpolation and extrapolation of the debris-flow surface within a region of interest (ROI) at $y = 5$ m (02:20 into the event). c) Interpolated channel base and inter- and extrapolated surface as in c), with measured cross-sectional area (α Shape; 11 m^2) and flow-depth based (z -threshold) at -4.8 m, to exclude points at the channel banks above the flow surface.

sectional area measurements, described above. Both datasets were synchronized by downsampling the measurements to 1 Hz. We derived the discharge for sections $y = 5$ m, $y = 10$ m, $y = 15$ m according to Eq. 1, and smoothed the results using a 10 s moving mean filter.

$$Q(y, t) = A(y, t) \cdot \bar{v}(y, t) = A(y, t) \cdot VF \cdot v_s(y, t) \quad (1)$$

where $Q(y, t)$ is the discharge at channel section y at event time t [m^3/s], $A(y, t)$ is the corresponding cross-sectional area (for a given channel geometry scenario; see also Fig. 6) [m^2], $\bar{v}(y, t)$ is the depth-averaged velocity [m/s] and VF is the velocity factor used to approximate the depth-averaged velocity by the surface velocity v_s [m/s], which was derived either using the camera1-ortho or the hillshade method.

The VF reduces the surface velocity according to the hypothesized vertical velocity profile, which has been investigated for this event in previous work of the authors (Aaron et al., 2023; Spielmann, 2022, summarized above). For the camera1-ortho based discharge measurements, we did not apply any depth-averaged correction (i.e. $VF = 1.00$) before 07:20, because we assume a plug-flow like velocity profile where the surface velocity roughly corresponds to the depth-averaged velocity (Aaron et al., 2023). After the arrival of the second surge and the “velocity jump” (see Sect. 2.3), we used a VF of 0.75 for the camera1-ortho method, a value slightly above to the velocity ratio between large, rolling boulders and pieces of woody debris (i.e. 0.6–0.7, cf. Aaron et al., 2023). We used a value slightly above this ratio, which represents the ratio between large boulders (\sim depth-averaged velocity) and the surface velocity (captured by the camera1-ortho approach, see also Sect. 2.3), to account for friction at the base and drag from the surrounding fluid on the boulders. This value is somewhat subjective, however it is bounded to a small range given the arguments above. For the discharge measurements based on the hillshade surface velocity, we did not apply any correction (i.e. $VF = 1.00$) because it is assumed that the velocities derived from the hillshade method approximate the depth-averaged velocity (Aaron et al., 2023; Spielmann, 2022).

3.5.2. Conventional event scale and surge scale discharge derivation

We estimated the discharge based on an event scale as well as a surge scale analysis to compare our new method to more commonly used methods (Lapillonne et al., 2023). For the first approach, we only consider the velocity of the flow front and assume it to represent the depth-averaged flow velocity for the entire event, which is an important assumption but commonly used to derive (peak) discharge and volumes (e.g. Marchi et al., 2021). For the second approach, which is based on an analysis of events on the surge scale as recently suggested by Lapillonne et al. (2023), we considered the front velocity (i.e. first surge) for the first phase of the event and the velocity of the second surge (after the “velocity jump”, i.e. after 07:20) for the second phase.

It is important to note that all of these measurements were based on the LiDAR data. In typical instrumented catchments, these measurements would come from travel time–distance velocity estimation methods and assumptions about the relationship between flow depth and the cross-sectional area (cf. Lapillonne et al., 2023). We therefore expect that our estimates are more accurate than those that would be typically used. Using the abovementioned parameters, we derived the discharge according to Eq. 2.

$$Q(t) = u \cdot A(t) \quad (2)$$

where $Q(t)$ is the discharge at event time t [m^3/s], u is the mean front and/or surge velocity [m/s] and $A(t)$ is the cross-sectional area at the crest of the check dam (i.e. $y = 0$ m) at t [m^2] (cf. also Lapillonne et al., 2023).

3.6. Event volume

The volume of the debris-flow event was calculated by integrating the discharge (at a given channel section, for a given channel geometry

scenario) over the entire duration of the event. Since the discharge values were not continuous but discrete (at a frequency of 1 Hz) in time (cf. e.g. Hübl and Mikoš, 2018), the total event volume was calculated as Riemann sum over subintervals of 1 s.

We derive three different discharge measurements (based on the pre-event, post-event and intermediate channel geometry; cf. also Fig. 6) for each of the three analyzed channel sections, for both velocity measurement techniques. Consequently, when applying our LiDAR-based method, we obtained nine volume values for each velocity dataset, which provides an idea of the uncertainty of our measurements. We hypothesize that the most accurate event volume is characterized by a value with the smallest discrepancy among the different sections, i.e. the median value, and therefore use this statistic to finally estimate event volume.

We compare the event volumes computed based on the instantaneous, LiDAR-based discharge analysis to volumes derived based on the conventional methods (event and surge scale discharge methodologies). For this purpose, we applied the same integration of the hydrographs described above.

4. Results

4.1. Front and surge velocities

Figure 7 shows the arrival of the debris-flow front of the 19 Sept. 2021 event in the channel segment upstream of the check dam and the LiDAR sensor. The flow front position was tracked in the LiDAR point clouds using both the manual and automated methods to derive the front velocity (Fig. 8). The same manual approach was applied to the second surge of the event to derive its velocity.

4.1.1. Manual front velocity measurement

Figure 8 shows the cumulative displacement of the flow front obtained from the manual measurements (Sect. 3.2.1 and Fig. 7). Two different trends in displacement are apparent, with a first phase occurring between 01:47–01:54, and a second phase occurring from 01:54–02:04. In the first phase, the velocity of the flow front (1.2 m/s) was greater than in the second phase (0.8 m/s), as can be seen from the linear fits to the data on Fig. 8.

4.1.2. Automated front velocity measurement

Figure 8 also shows the cumulative displacement of the front based on the automated debris-flow front detection technique. The automated results show a similar trend as the manual method, i.e. a change in the displacement rate from a first to a second phase. Nevertheless, as indicated by the trendlines, the automatically derived front velocity in the first phase (1.1 m/s) was slightly slower than the manual front velocity in the same phase. However, in the second phase, the automatically derived velocity was similar to the manual measurements (i.e. 0.8 m/s).

4.1.3. Velocity of the second surge

As mentioned above and by Aaron et al. (2023), the 19. Sept. 2021 event was characterized by a second surge at around 07:20. The velocity of this surge was measured manually by tracking a piece of woody debris, which was located at the head of the second surge (see feature labels in Fig. SI 2). The mean velocity of the log and thus the surge in the channel segment upstream of the check dam was around 2.5 m/s. This velocity will be used for the conventional surge scale discharge derivations (see also Table SI 1).

4.2. Surface velocity

The average surface velocity across each of the three channel sections over time is shown in Fig. 9a and Fig. 9b for the camera1-ortho and the hillshade methods, respectively. The measured surface velocities vary substantially in time and space. The camera1-ortho-based results

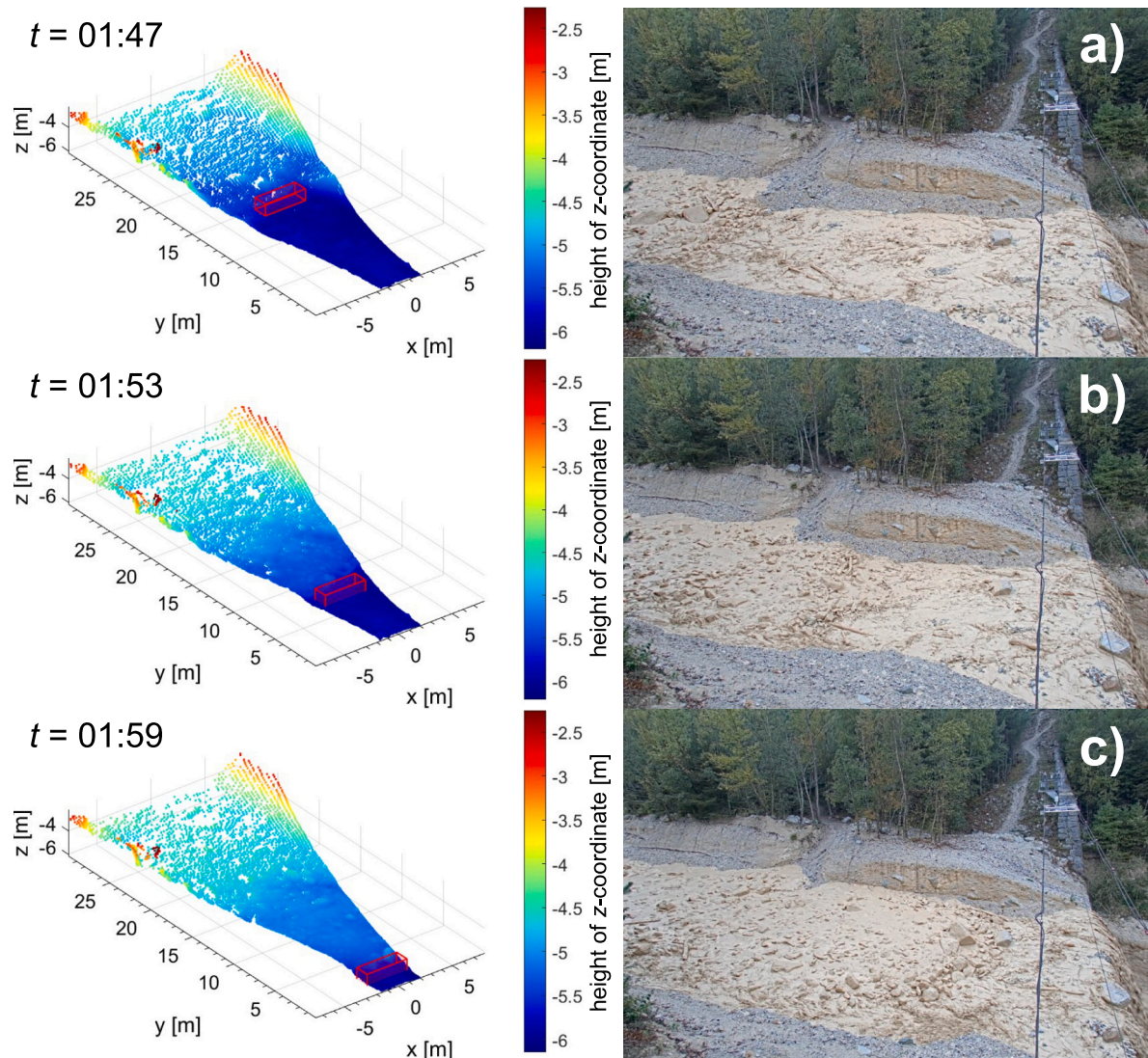


Fig. 7. Point clouds (left; colored according to height of z-coordinate) and video images (right) of the front arrival upstream of the 19 Sept. 2021 event just upstream of the check dam and LiDAR sensor. The flow front was tracked manually (red box) in the point clouds to derive its velocity.

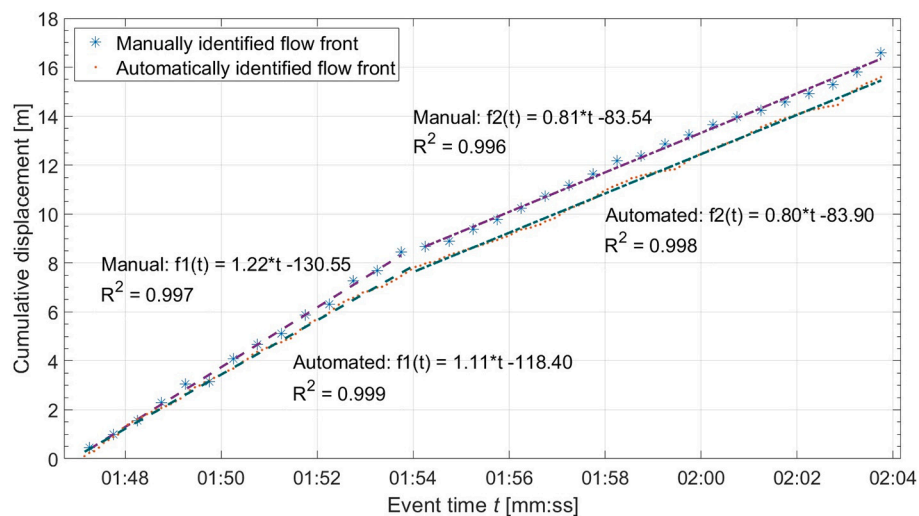


Fig. 8. Trajectory of the front from the 19 Sept. 2021 debris flow, manually (every 0.5 s) and automatically (every 0.1 s) identified in the LiDAR point-cloud frames over the channel segment ca. 25 m upstream of the check dam. The slopes of the trendlines indicate the front velocity.

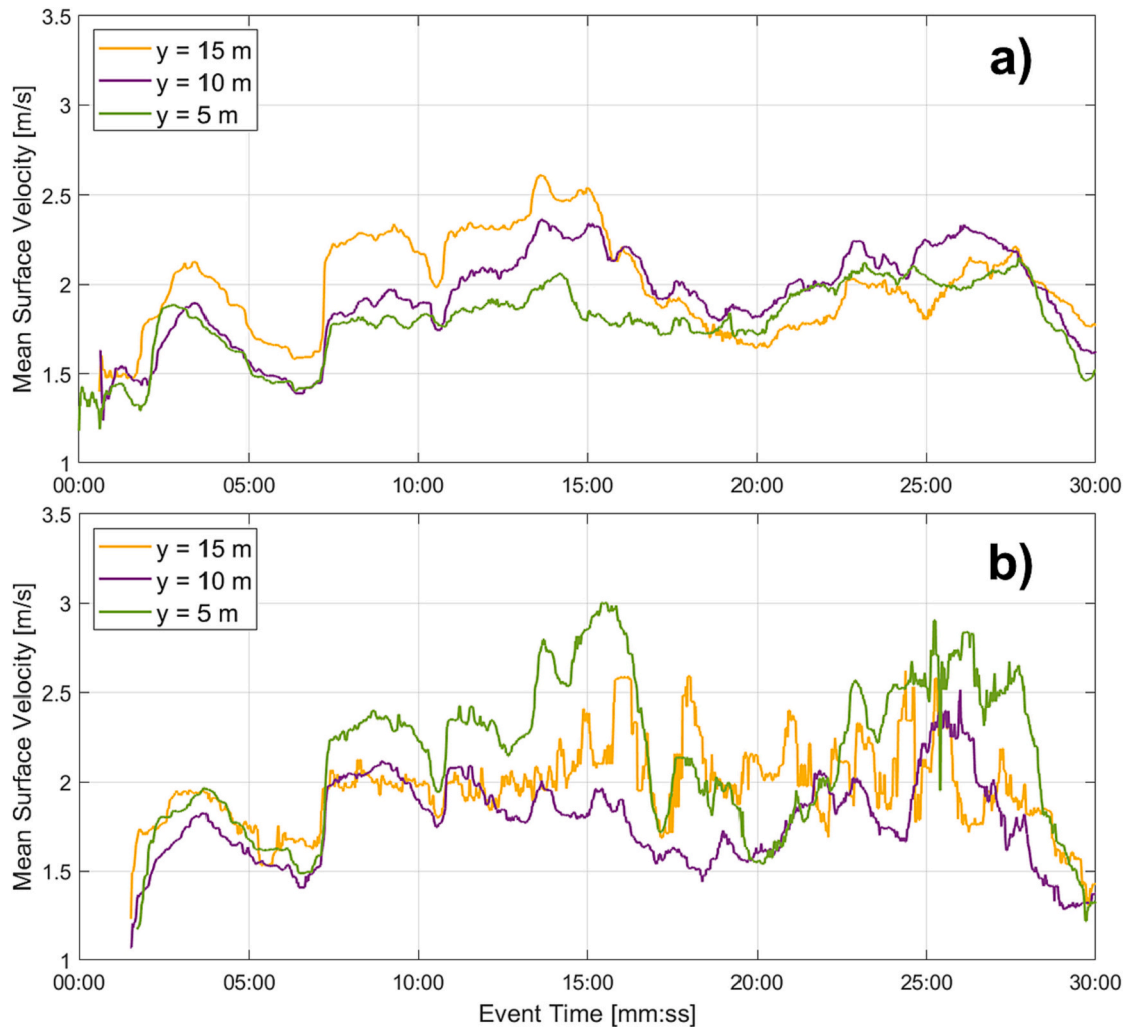


Fig. 9. Automated surface velocity measurements for three selected channel sections (upstream of sensor distance y ; Fig. 5) based on a) camera1-ortho and b) hillshade surface velocity measurement methods (see Sect. 3.3) for the 19 Sept. 2021 debris flow. The values shown here for each channel section represent average values across the entire section for a given time and were smoothed with a moving median over 30 s.

show two sharp increases in the velocity by ca. 0.5 m/s: the first one (at ca. 03:00) after the front arrival (which occurs roughly at 02:00 at the check dam, cf. Fig. 8) and the second one with the arrival of the second surge (ca. 07:20; Fig. 9a). However, the surface velocities measured at the different channel sections differ by up to 0.5 m/s (ca. 20%), with the section at $y = 15$ m showing faster velocities than at $y = 10$ m and $y = 5$ m, i.e. we can observe a slight deceleration towards the check dam in Fig. 9a.

The results from the hillshade method show the same temporal pattern described above. Furthermore, the velocities measured at the different sections are in relatively good agreement over the first 07:20 of the event, i.e. before the arrival of the second surge. However, after 07:20, substantially faster velocities (ca. 0.2 m/s to 1 m/s) are measured at $y = 5$ m in comparison to sections $y = 10$ m and $y = 15$ m, i.e. an acceleration of the surface velocity towards the check dam can be observed (see also Fig. SI 2). This discrepancy between the two velocity measurement methods will be discussed below.

4.3. Cross-sectional area

The cross-sectional area of the 19 Sept. 2021 event was measured at six channel sections upstream of the LiDAR sensor, considering the previously described channel geometry scenarios. In Fig. 10, we show the results of these cross-sectional area measurements based on the

intermediate channel geometry scenario. The measurements based on the other scenarios (i.e. pre-event and post-event), which provide an idea of the uncertainty of our measurements, can be found in the Supplementary Information (Fig. SI 6) along with an overview of the shape of the channel bed according to the three channel geometry scenarios for each channel section (Fig. SI 4 and Fig. SI 5).

All cross sections show a similar temporal trend (Fig. 10). A first peak in the cross-sectional area is observed shortly after 02:00, followed by a decrease in the area up to the second surge arrival at 07:20, which is then followed by a final, steady decrease in the cross-sectional area towards the end of the event. However, as indicated in Fig. 10, the absolute values of the cross-sectional area measured for the different channel sections vary substantially among the different sections: We can observe a clear decrease in the cross-sectional area of the flow towards the sensor, i.e. towards the check dam.

4.4. Discharge

Figure 11 shows the LiDAR-based discharge hydrographs for the three analyzed channel sections based on the different channel geometry scenarios at each section and the two velocity measurement methods. Furthermore, as a comparison, we show results from conventional discharge methodologies based on the mean front velocity (Fig. 11c, event scale analysis) as well as based on the front and second surge

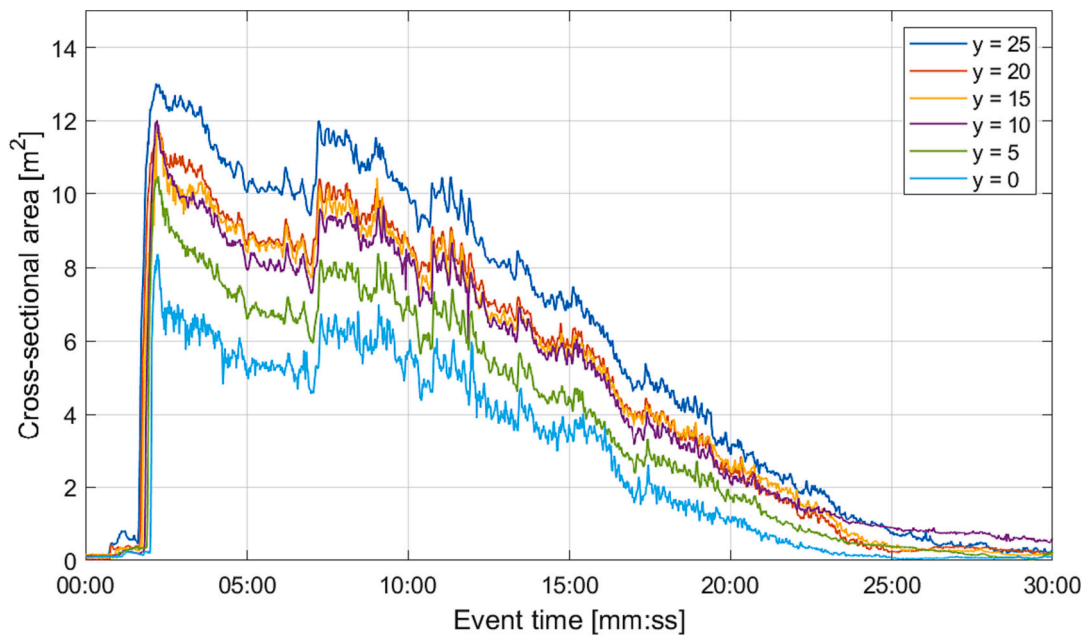


Fig. 10. Cross-sectional area of the 19 Sept. 2021 event at different channel sections upstream of the LiDAR sensor (upstream of sensor distance y in meters; Fig. 5). The shown values are based on the intermediate channel geometry (Fig. 6) and were smoothed (mean over 1 s window) for visualization purposes. The full range of cross-sectional area values, based on the pre- and post-event channel geometry scenarios, can be found in Fig. SI 6.

velocities (Fig. 11d, surge scale analysis).

The results from the camera1-ortho method (Fig. 11a) clearly show the arrival of the front, with peak discharge values between $18 \text{ m}^3/\text{s}$ and $21 \text{ m}^3/\text{s}$ (intermediate channel geometry). After the arrival of the second surge, where we applied a velocity factor (see Sect. 3.5.1) and where we measured a discharge between $11 \text{ m}^3/\text{s}$ and $16 \text{ m}^3/\text{s}$, the discrepancy among different sections is ca. $2 \text{ m}^3/\text{s}$, with a decrease in the measured discharge towards the check dam (i.e. from $y = 15$ to $y = 5$), an important observation that will be discussed later.

The hillshade method provides discharge values of $17 \text{ m}^3/\text{s}$ – $20 \text{ m}^3/\text{s}$ (intermediate channel geometry) for the phase of the front arrival. The different sections agree reasonably well over the first phase of the event (i.e. up to 07:20), but the section at $y = 5 \text{ m}$ is consistently lower than the other two sections. During the arrival of the second surge, we measured greater values ($17 \text{ m}^3/\text{s}$ – $19 \text{ m}^3/\text{s}$) than for the camera1-ortho based discharge, which might also be related to the applied velocity factor of 0.75, as will be discussed below.

For the conventional event scale and surge scale discharge methods we considered the front and surge velocities provided in the Supplementary Information (Table SI 1 and Fig. SI 2) in combination with the cross-sectional area measurements provided above (Fig. 10). Both of these methods provide much lower peak discharges than that provided by the LiDAR-based method, with values for the first phase of around $8 \text{ m}^3/\text{s}$ (Fig. 11c and Fig. 11d). For the second phase (i.e. after 07:20), the discharge amounts to roughly $7 \text{ m}^3/\text{s}$ for the front-velocity based estimates (Fig. 11c) and to ca. $16 \text{ m}^3/\text{s}$ for the surge scale analysis (Fig. 11d).

4.5. Event volume

We derived the volume of the 19 Sept. 2021 debris flow based on the discharge hydrographs presented in Fig. 11. The results are shown in Fig. 12. Based on the three different channel geometry scenarios for each of the three sections, we obtain three volume values for each section, as mentioned above. As we expect mass to be conserved over such a short distance, the most realistic volume is a value that is in agreement among the different sections. Therefore, as mentioned above, we derived the median of these volumes, which is a best fit value for the volume of this

event at this location. These median volumes are also indicated in Fig. 12 and amount to $12,180 \text{ m}^3$ for camera1-ortho and $14,680 \text{ m}^3$ for the hillshade method. Reasons for this observed discrepancy of 2500 m^3 between the two velocity methods will be provided below. Fig. 12 also shows the volume estimates based on the conventional event scale and surge scale approaches. The mean (i.e. based on the intermediate channel geometry) volumes amount to 4960 m^3 and 9600 m^3 and are thus substantially lower than for the instantaneous, LiDAR-based discharge approach presented in this work.

It is interesting to note that, for the camera1-ortho method, the median value is closest to the pre-event at $y = 5 \text{ m}$, the intermediate at $y = 10 \text{ m}$, and the post-event channel geometry at $y = 15 \text{ m}$. The hillshade approach indicates a similar pattern, with the exception of the intermediate channel geometry at $y = 5 \text{ m}$ being closer to the median than the pre-event channel geometry (Fig. 12). We will discuss what we can infer from this observation about the evolution of the channel bed and its geometry below.

5. Discussion

5.1. Front and surge velocities

Front velocity is an important parameter for conventional approaches to estimate discharge. Our high temporal resolution manual and automatic measurements show an observed decrease in the front velocity by ca. 0.4 m/s (33%) over the investigated channel segment (Fig. 8). We explain this by a change in the channel slope and a widening of the channel cross section. For the 19 Sept. 2021 event, the mean channel slope in the segment 10 m to 20 m upstream of the sensor was 4.2° and the channel width was 7 m–9 m, whereas in the segment from 0 m to 10 m the slope reduced to 1.9° and the channel width increased to 12 m–14 m (Spielmann, 2022). We observe that, during the first phase of the front arrival the automated method provided a roughly 0.1 m/s slower velocity than the manual approach. A possible explanation for this discrepancy between the two methods could be the selection and application of a (fixed) geometrical threshold.

These observations show that the velocity of the front of a debris flow is strongly affected by the channel geometry, even over a relatively short

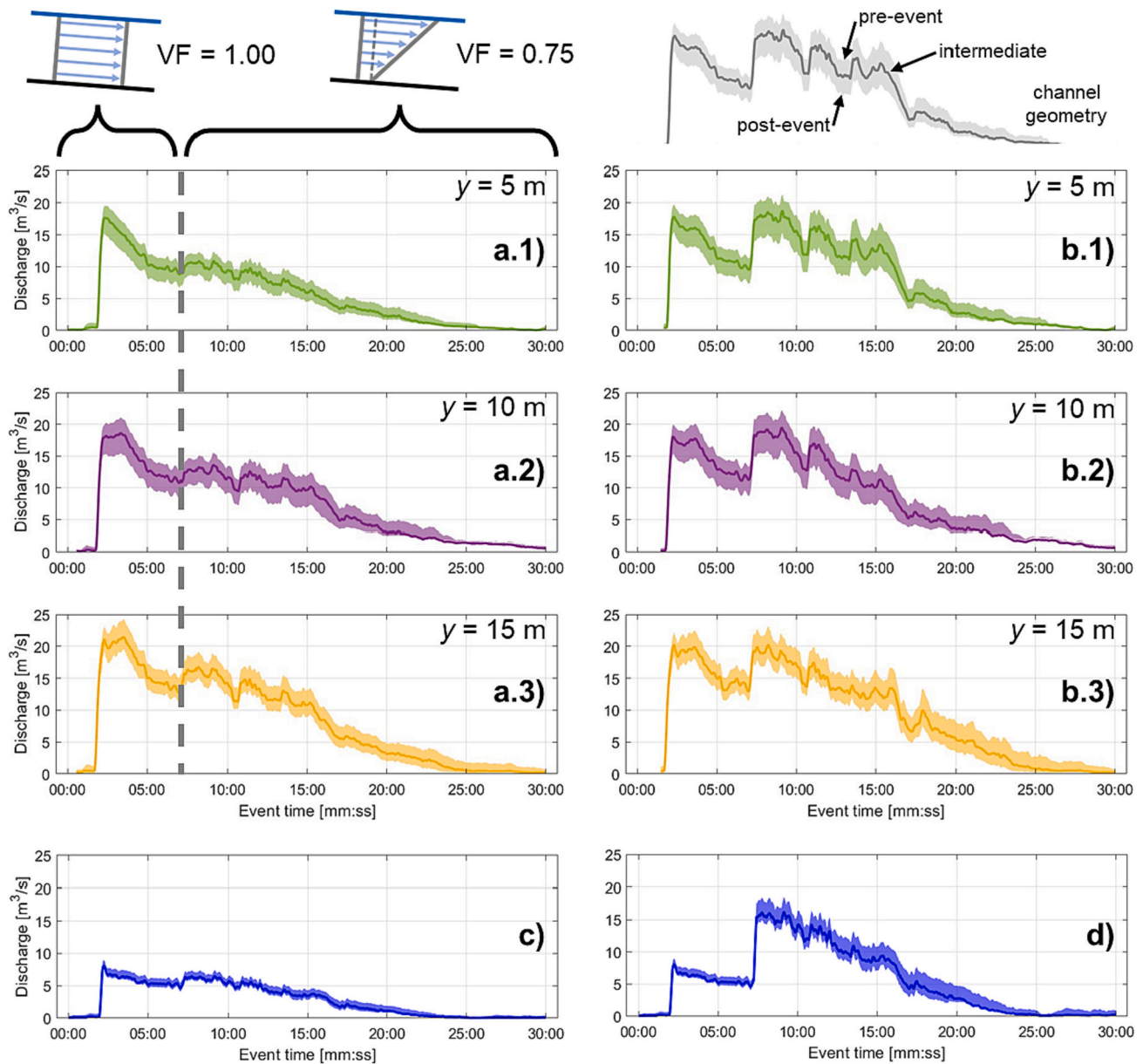


Fig. 11. Discharge hydrographs for a) camera1-ortho (with a velocity factor $VF = 1.00$ before 07:20 and with $VF = 0.75$ after 07:20, i.e., plug-flow like and with internal shearing, respectively, as indicated with the conceptual velocity profiles on top and as described in Sect. 3.5) and b) hillshade (velocity factor = 1.00) based velocity measurements at different channel sections (Fig. 5). As a comparison, we show discharge estimates from conventional methods for a section below the sensor ($y = 0$ m) based on c) front velocity measurements (event scale approach) as well as d) front and surge velocity measurements (surge scale approach; see also Table SI 1).

channel segment. Such changes of the front velocity are usually not detected by conventional monitoring setups where the (mean) front velocity is assessed from the travel time between a pair of sensors, especially if they are located at a relatively large distance from each other (e.g. Hürlimann et al., 2019; Lapillonne et al., 2023). Further, estimating the velocity of the second surge based on conventional (stage) measurement techniques would require correlating changes in flow depth of around 10 cm to 20 cm. As show in Fig. 11, it is crucial to have this velocity for the derivation of discharge according to the surge scale approach (Lapillonne et al., 2023).

5.2. Surface velocity

Continuous measurements of the debris-flow (surface) velocity over the entire event are crucial for our new, LiDAR-based discharge

methodology. Due to this importance, we developed and assessed two different methods (camera1-ortho and hillshade). We observed a decrease in surface velocity towards the check dam in the camera1-ortho-based measurements (Fig. 9a), which might be related to the change in the shape of the channel, described in the previous section. Similar to the front velocity, higher velocities are expected in the narrower and steeper segment of the channel (i.e. for the section at $y = 15$ m) than in the wider and flatter segment (i.e. for $y = 5$ m and $y = 10$ m). This was not observed in the hillshade-based velocities (Fig. 9b), which is likely related to the field of view of the LiDAR sensor: whereas camera1 records the full width of the channel segment upstream of the check dam, the LiDAR sensor's field of view – in particular close to the check dam – is limited to the channel middle where velocities are highest (see also Fig. 5 and Fig. SI 1). During the first phase of the event (up to 07:20, see Fig. 9b), the discrepancy among surface velocities at different

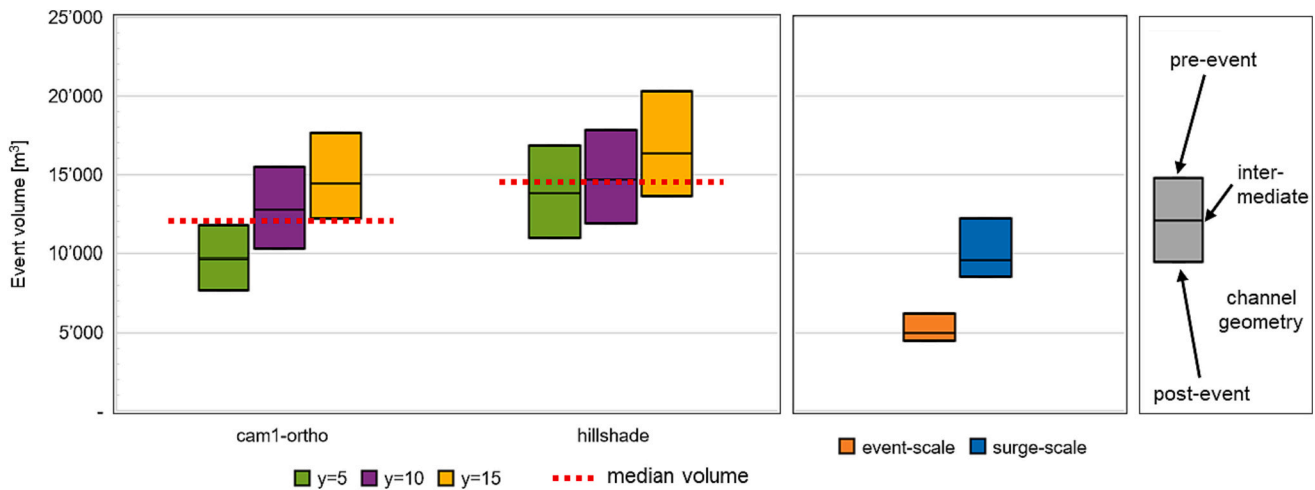


Fig. 12. Event volumes for the 19 Sept. 2021 debris flow, based on the discharge hydrographs presented in Fig. 11. The resulting median volumes are 12,180 m³ for camera1-ortho and 14,680 m³ for the hillshade method (dashed red lines), as well as 4960 m³ and 9600 m³ (intermediate value) for the event scale and surge scale discharge analysis (see Fig. 11c Fig. 11d).

sections was only minor, which indicates that the velocities must be relatively constant across the entire channel width so that the “sampling width” has no effect on the resulting hillshade velocities.

This hypothesis is in good agreement with observations from Aaron et al. (2023), who suggested a change in the vertical velocity profile from block sliding to a velocity profile that features internal shearing for the 19 Sept. 2021 event. Even though further investigations of these debris-flow velocities are required, such a change in the vertical velocity profile could likely affect the horizontal (transverse) velocity profile (e.g. Han et al., 2014), and thus explain the abovementioned observation for the hillshade method. As suggested by Aaron et al. (2023), the change in the velocity profile itself could be linked to a change in the concentration of coarse particles and/or a change in the water content of the flow.

5.3. Cross-sectional area

Cross-sectional area is the second crucial parameter for estimating discharge, and we observe a surprising decrease in cross-sectional area towards the check dam (Fig. 10). This observed decrease exceeds the uncertainty related to changes in the channel bed (from pre-event to post-event; see Fig. SI 6). A potential explanation for this could be a decreasing flow depth close to check dams analogous to the hydraulic drawdown effect observed in river flow (e.g. Henderson, 1966). Nevertheless, this systematic decrease of cross-sectional area towards the check dam has important implications for conventional monitoring systems because flow depth sensors in many cases are located directly above check dams (cf. e.g. Hürlimann et al., 2019) and thus estimate the (equivalent) cross-sectional area at this location. Eventually, this will have an impact on conventional discharge estimates based on measurements from such sensors, as detailed below.

Furthermore, we acknowledge that our cross-sectional method cannot account for situations where the debris flow erodes below the pre- and post-event channel geometry, and then subsequently deposits. Although this likely occurs in debris flows (cf. Berger et al., 2011a), we think it is a minor source of uncertainty in the present work as our cross sections are located immediately upstream of a check-dam, which should stabilize the channel bed (see Fig. 5).

5.4. Discharge

Discharge is a fundamental parameter for practical hazard assessment and to describe debris-flow motion, and we have measured it at

very high spatial and temporal resolution using our LiDAR-based method. As a comparison, we furthermore estimated the discharge using more conventional methodologies based on event scale and surge scale velocity analyses (Fig. 11).

For the discharge estimates from the camera-based velocities, our high-resolution discharge measurements show a surprising trend of decreasing discharge towards the sensor, i.e. towards the check dam over the entire duration of the event (Fig. 11a). This observation is paradoxical, as mass should be conserved over such a short distance (10 m), and we could not observe any major deposition during the event in the videos. There are two main explanations for this observed discrepancy: 1) changes in the channel bed geometry during the event and/or 2) changes in the velocity profile along the channel. The first factor can account for the majority of this discrepancy if we consider the pre-event geometry for the channel section at $y = 5$ m, intermediate geometry for $y = 10$ m, and post-event geometry for $y = 15$ m (cf. Fig. 12). This would indicate that the channel geometry changed to its post-event configuration at each of these sections at different times during the event.

However, a discrepancy of ca. 1 m³/s – 3 m³/s remains (between $y = 5$ m and $y = 15$ m), even if we consider the abovementioned scenarios. This discrepancy is likely related to the second factor, i.e. spatial (in addition to temporal) changes in the velocity profile along the channel. Such a spatial change in the vertical velocity profile, e.g. from shear with less basal slip at $y = 15$ m to shear with more basal slip and thus a greater depth-averaged velocity at $y = 5$ m (after 07:20), could explain the remaining discrepancy. A more quantitative analysis and further work are required to analyze such along channel velocity profile changes in more detail.

The results of the hillshade-based discharge analysis show a smaller discrepancy among the sections (max. 1 m³/s for sections $y = 5$ m and $y = 15$ m, considering pre- and post-event channel geometries, respectively; cf. Fig. 12) and only during the first surge of the event (Fig. 11b). As the hillshade velocities likely approximate the depth-averaged velocity of the flow they account for temporal and spatial changes in the velocity profile (\neq camera1-ortho method). We can thus conclude that this remaining discrepancy is mainly related to channel bed geometry changes above or below the channel geometry scenarios assumed here.

5.4.1. Comparison with conventional discharge methods

We compare the results from our new LiDAR-based method to more conventional methodologies, which are based on mean velocity assumptions (either at the event scale or at the surge scale; Lapillonne et al., 2023). We find that the event scale analysis, where the front

velocity is used as mean velocity for the entire event, likely underestimates the discharge for most of the event (Fig. 11c). In particular, the peak discharges of the front and the second surge are roughly $10 \text{ m}^3/\text{s}$ (60%) smaller than based on our instantaneous, LiDAR-based method. The underestimation of the peak discharge during the first phase using the (mean) front velocity is mainly related to the fact that the velocities behind the front are around $1.5\times$ faster than the front itself, as documented by Aaron et al. (2023) for this event and as observed similarly for other events by other researchers (e.g. Jacquemart et al., 2017; Suwa et al., 1993). For the surge scale analysis, we make the same observation for the first phase of the event, as we used the same front velocity to derive the discharge (Fig. 11d). For the second phase of the event, however, the agreement with the other two methods is better as we used the velocity of the second surge, which is substantially higher (2.5 m/s) than the front velocity (ca. 1.0 m/s). These differences in the discharge hydrographs have substantial implications for the volume derivation, which will be discussed below.

5.5. Event volume

Debris-flow volume is one of the most important parameters for hazard assessment and is often estimated using empirical equations (Rickenmann, 1999) or conventional discharge estimates (Lapillonne et al., 2023). In this work, we have presented volume estimates for the 19 Sept. 2021 debris flow, which were derived from our detailed LiDAR-based discharge methodology. The different channel geometry scenarios resulted in a range of volume values for different sections (Fig. 12). However, as mentioned above for the discharge, it seems unlikely that the volume would change between these sections. We therefore assume that the median value over the different sections is the “best-fit” volume value among the sections, i.e. the best approximation of the actual event volume. As discussed above, considerations of conservation of mass allow us to conclude which of the channel geometry scenarios is the most appropriate for each channel section. Based on our findings, the post-event at $y = 15 \text{ m}$ and the intermediate channel geometry at $y = 10 \text{ m}$ are the scenarios closest to the median value (cf. Fig. 12). We therefore infer that the cross-sectional area at $y = 15 \text{ m}$ and $y = 10 \text{ m}$ was reduced in this event by deposition early in the event (see also Fig. SI 4 and Fig. SI 5). For the section closest to the check dam, i.e. $y = 5 \text{ m}$, the situation is less clear as the two different methods provide slightly different results. Nonetheless, we can infer that the channel geometry was (similar or equivalent) to a shape somewhere in between the pre-event or intermediate channel geometry scenario for most of the event, and deposition only occurred relatively late. Future analyses will investigate these preliminary findings further and expand them to more events.

The median volume for the camera1-ortho method ($12,180 \text{ m}^3$) is smaller than the median volume for the hillshade based approach ($14,680 \text{ m}^3$). This discrepancy is mainly related to differences in the estimated discharge during the second surge, whereas the peak discharges for the first surge (front arrival) agreed quite well (cf. Fig. 11). The differences during the second surge could partially be due to the selected velocity factor during the second phase ($VF = 0.75$) for the camera-based approach. Even though this factor is based on velocity measurements, i.e. the velocity ratio between large, rolling boulders and woody debris of the 19 Sept. 2021 event (see Sect. 2.3, Fig. SI 2 and Aaron et al., 2023), some uncertainty remains in the selection of this value. Nonetheless, other researchers have used similar values (e.g. 0.6, cf. Cui et al., 2018; Suwa et al., 1993). In contrast, the hillshade method is not subject to this limitation, and might thus be the most reliable, however it is limited by the field of view of the LiDAR, as described above.

5.5.1. Comparison with conventional event volume approaches

As shown in Fig. 12, we compared the results from our LiDAR-based approach to volume estimates from conventional methods. No other

independent comparison was possible, as the debris flows at the Illgraben directly flow into the Rhone River (cf. Fig. 1) and the deposited volume cannot be measured after events.

As expected from the hydrographs (Fig. 11), the conventional event and surge scale methodologies substantially underestimate the event volume (Fig. 12). The event scale analysis, which used the front velocity over the entire event, provides an event volume (intermediate scenario) which is over $10,000 \text{ m}^3$ smaller than the hillshade-based (median) volume, i.e. only corresponds to $1/3$ of that volume. The surge scale analysis, which in addition to the front velocity considered the velocity of the second surge to derive the hydrograph, provides a volume 40%, i.e. over 5000 m^3 (intermediate scenario), smaller than the (median) hillshade volume (Fig. 12). The main cause for the discrepancy between this approach and the hillshade method is the substantial underestimation of the first phase of the event due to the small front velocity (cf. also Aaron et al., 2023 and Fig. SI 2).

Furthermore, it should be mentioned that the inputs used in this work for the two conventional approaches, which are based on high-frequency LiDAR measurements, are likely much more accurate than in a traditional monitoring system with classical instruments such as geophones or depth sensors. In particular the cross-sectional area can usually not be measured directly in such great detail as in this study, but has to be inferred (indirectly) from a relationship between the flow height and the wetted area (cf. Lapillonne et al., 2023). Additionally, the identification of the second surge would likely not have been successful if geophones were used, as the second surge was a very subtle feature in terms of flow depth (flow height change of only a $10 \text{ cm} - 20 \text{ cm}$), but not when it comes to velocity as the velocity more than doubled (compared to the front velocity). Therefore, the results for the conventional methodologies presented here represents a “best-case” scenario, but one that would be extremely difficult to achieve in the absence of a high-resolution 3D LiDAR sensor.

6. Conclusions

We used a new high-resolution, high-frequency 3D laser scanner (LiDAR) to record a debris flow that occurred on 19 Sept. 2021 in the Illgraben. We analyze sub-second timelapse point-cloud data from a 25 m long channel segment upstream of a check dam on the debris-flow fan to measure important parameters such as i) front velocity, ii) surge velocity, iii) surface velocity and iv) cross-sectional area. Based on these detailed measurements, we derive instantaneous estimates of the discharge and calculate the event volume. The main findings of our work can be summarized as follows:

1. Debris flow front velocity is sensitive to changes in both channel slope and channel width. These factors likely resulted in a decrease of the front velocity (from 1.2 m/s to 0.8 m/s) over a relatively short ($\sim 20 \text{ m}$) channel segment.
2. In this event, the velocity of the second surge, which arrives at $\sim 7 \text{ min}$, had a substantially higher velocity than the front (2.5 m/s on average). This leads to a substantial underestimation of (peak) discharge if the front velocity is used to derive this parameter.
3. Similar to Aaron et al. (2023), the new analyses and detailed comparisons presented here suggest a temporal change in the vertical velocity profile from block sliding to a velocity profile that features internal shearing in the second phase. We further suggest a spatial change of this velocity profile (after 07:20) towards the check dam, e.g. from one with less basal slip to one with more basal slip and thus a greater depth-averaged velocity close to the check dam.
4. We observe a surprising decrease in the cross-sectional area towards the check dam (e.g. by 40% from 25 m to 0 m upstream of the sensor), which exceeds the uncertainty related to the different channel geometry scenarios, likely explained by the hydraulic drawdown effect observed upstream of a free overfall open channel flow (e.g. Henderson, 1966). This observation has important

implications for conventional monitoring systems located at check dams (e.g. depth sensors suspended above the crest), as these systems usually consider (a virtual equivalent) of the cross-sectional area directly at the check dam and thus – based on the findings from this work and this event – likely underpredict the cross-sectional area and thus the discharge.

5. We developed a new LiDAR-based methodology to derive discharge and compared it to conventional methods. These methods substantially underestimate the (peak) discharge of the event, e.g. by ca. 60% for the front arrival. Using a surge scale approach, as suggested by Lapillonne et al. (2023), can improve this if surge velocities can be accurately estimated.
6. We derived the volume of the 19 Sept. 2021 event based on the LiDAR-based discharge hydrographs for the different channel geometry scenarios and channel sections, which provided an idea of the uncertainties. As mass should be conserved over such a short channel segment (10 m) and no signs of continuous material deposition are shown in the videos, we assume that the most representative volume is the median over all sections, and that deposition occurred early in the event for the more upstream channel sections.
7. A comparison of our results (median volumes 12,180 m³ for camera1-ortho and 14,680 m³ for the hillshade method) to volume estimates based on the conventional approaches (intermediate values of 4960 m³ and 9600 m³ for the event scale and surge scale analysis, respectively) revealed that these methods substantially underestimate the volume for the event analyzed in this work.

Even though the findings of the present study need to be assessed in the future by analyzing more events, our instantaneous, LiDAR-based method has the potential to provide much more detailed and accurate information on hazard-related debris-flow parameters. In particular, it allows for high spatial and temporal resolution field-scale measurements of (peak) discharge and volume, which are currently not available for debris flows. This will help us to improve our understanding of these hazardous processes and allow for a better hazard management in the future.

CRedit authorship contribution statement

Raffaele Spielmann: Writing – review & editing, Writing – original draft, Visualization, Software, Methodology, Investigation. **Jordan Aaron:** Writing – review & editing, Visualization, Validation, Supervision, Software, Resources, Project administration, Methodology, Funding acquisition, Conceptualization.

Declaration of Competing Interest

The authors declare the following financial interests/personal relationships which may be considered as potential competing interests:

Jordan Aaron reports financial support was provided by Swiss National Science Foundation.

Data availability

The data underlying this publication can be found in the ETH Research Collection under doi:10.3929/ethz-b-000620259. Additional data for the same debris-flow event (19 September 2021), analyzed by Aaron et al. (2023), can be found under doi:10.3929/ethz-b-000599948. The workflow used in this project is based on the following software: Automated velocity measurements: PIV-Lab, <https://www.mathworks.com/matlabcentral/fileexchange/27659-pivlab-particle-image-velocity-piv-tool-with-gui> (Thielicke and Sonntag, 2021). Projection of point clouds to hillshades: Hillshade function, <https://www.mathworks.com/matlabcentral/fileexchange/32088-esri-hillshade-algorithm>. Point-cloud visualization: CloudCompare, <https://www.danielgm.net/cc/>.

Acknowledgements

This work was funded by the Swiss National Science Foundation (SNSF) [grant number 193081] as well as funds from the Chair of Engineering Geology at ETH Zürich. We are grateful for technical support as well as scientific advice from Stefan Boss (WSL), Christoph Graf (WSL), Dr. Brian McArdell (WSL) as well as Dr. Jacob Hirschberg (WSL/ETH). We would like to thank Prof. Dr. Tjalling de Haas (Utrecht University) for providing digital terrain data from UAV flights. We are grateful to the editor for coordinating and to three anonymous reviewers for their constructive feedback that improved this manuscript.

Appendix A. Supplementary data

Supplementary information to this article can be found online at <https://doi.org/10.1016/j.enggeo.2023.107386>.

References

- Aaron, J., Spielmann, R., McArdell, B.W., Graf, C., 2023. High-frequency 3D LiDAR Measurements of a Debris Flow: a Novel Method to Investigate the Dynamics of Full-Scale events in the Field. *Geophys. Res. Lett.* 50 <https://doi.org/10.1029/2022GL102373>.
- Andres, N., Badoux, A., 2019. The Swiss flood and landslide damage database: normalisation and trends. *J. Flood Risk Manag.* 12 <https://doi.org/10.1111/jfr3.12510>.
- Arattano, M., Marchi, L., Cavalli, M., 2012. Analysis of debris-flow recordings in an instrumented basin: confirmations and new findings. *Nat. Hazards Earth Syst. Sci.* 12, 679–686. <https://doi.org/10.5194/nhess-12-679-2012>.
- Badoux, A., Graf, C., Rhyner, J., Kuntner, R., McArdell, B.W., 2009. A debris-flow alarm system for the Alpine Illgraben catchment: design and performance. *Nat. Hazards* 49, 517–539. <https://doi.org/10.1007/s11069-008-9303-x>.
- Bennett, G.L., Molnar, P., McArdell, B.W., Schlunegger, F., Burlando, P., 2013. Patterns and controls of sediment production, transfer and yield in the Illgraben. *Geomorphology* 188, 68–82. <https://doi.org/10.1016/j.geomorph.2012.11.029>.
- Berger, C., McArdell, B.W., Schlunegger, F., 2011a. Direct measurement of channel erosion by debris flows, Illgraben, Switzerland. *J. Geophys. Res. Earth Surf.* 116, 148–227. <https://doi.org/10.1029/2010JF001722>.
- Berger, C., McArdell, B.W., Schlunegger, F., 2011b. Sediment transfer patterns at the Illgraben catchment, Switzerland: implications for the time scales of debris flow activities. *Geomorphology* 125, 421–432. <https://doi.org/10.1016/j.geomorph.2010.10.019>.
- Chen, N.S., Yue, Z.Q., Cui, P., Li, Z.L., 2007. A rational method for estimating maximum discharge of a landslide-induced debris flow: a case study from southwestern China. *Geomorphology* 84, 44–58. <https://doi.org/10.1016/j.geomorph.2006.07.007>.
- Comiti, F., Marchi, L., Macconi, P., Arattano, M., Bertoldi, G., Borga, M., Brardinoni, F., Cavalli, M., D'Agostino, V., Penna, D., Theule, J., 2014. A new monitoring station for debris flows in the European Alps: first observations in the Gadría basin. *Nat. Hazards* 73, 1175–1198. <https://doi.org/10.1007/s11069-014-1088-5>.
- Coviello, V., Theule, J.L., Crema, S., Arattano, M., Comiti, F., Cavalli, M., Lucía, A., Macconi, P., Marchi, L., 2020. Combining Instrumental monitoring and high-resolution topography for estimating sediment yield in a Debris-Flow Catchment. *Environ. Eng. Geosci.* 27, 95–111. <https://doi.org/10.2113/EEG-D-20-00025>.
- Cui, P., Guo, X., Yan, Y., Li, Y., Ge, Y., 2018. Real-time observation of an active debris flow watershed in the Wenchuan Earthquake area. *Geomorphology* 321, 153–166. <https://doi.org/10.1016/j.geomorph.2018.08.024>.
- Dowling, C.A., Santi, P.M., 2014. Debris flows and their toll on human life: a global analysis of debris-flow fatalities from 1950 to 2011. *Nat. Hazards* 71, 203–227. <https://doi.org/10.1007/s11069-013-0907-4>.
- Graf, C., Badoux, A., Dufour, F., Fritsch, B., McArdell, B.W., Rhyner, J., Kuntner, R., Teyssie, P., Nigg, U., 2007. Alarmsystem für murgangfähige Wildbäche–Beispiel Illgraben. *Wasser Energ. Luft* 99, 119–128.
- de Haas, T., McArdell, B.W., Nijland, W., Åberg, A.S., Hirschberg, J., Huguénin, P., 2022. Flow and bed conditions jointly control debris-flow erosion and bulking. *Geophys. Res. Lett.* 49 <https://doi.org/10.1029/2021GL097611> e2021GL097611.
- Han, Z., Chen, G., Li, Y., Xu, L., Zheng, L., Zhang, Y., 2014. A new approach for analyzing the velocity distribution of debris flows at typical cross-sections. *Nat. Hazards* 74, 2053–2070. <https://doi.org/10.1007/s11069-014-1276-3>.
- Henderson, F.M., 1966. *Open Channel Flow*. Macmillan, New York.
- Hirschberg, J., Fatichi, S., Bennett, G.L., McArdell, B.W., Peleg, N., Lane, S.N., Schlunegger, F., Molnar, P., 2021. Climate change impacts on sediment yield and debris-flow activity in an alpine catchment. *J. Geophys. Res. F Earth Surf.* <https://doi.org/10.1029/2020JF005739>.
- Hübl, J., Mikos, M., 2018. TXT-tool 2.386-1.2: Practice guidelines on monitoring and Warning Technology for Debris Flows. In: Sassa, K., Guzzetti, F., Yamagishi, H., Arbanas, Z., Casagli, N., McSaveney, M., Dang, K. (Eds.), *Landslide Dynamics: ISDR-ICL Landslide Interactive Teaching Tools : Volume 1: Fundamentals. Mapping and Monitoring*. Springer International Publishing, Cham, pp. 567–585. https://doi.org/10.1007/978-3-319-57774-6_41.

- Hübl, J., Schimmel, A., Koschuch, R., 2018. Evaluation of different methods for debris flow velocity measurements at the Lattenbach Creek. In: Presented at the Interpraevent 2018 in the Pacific Rim, Toyama, Japan.
- Hungr, O., Leroueil, S., Picarelli, L., 2014. The Varnes classification of landslide types, an update. *Landslides* 11, 167–194. <https://doi.org/10.1007/s10346-013-0436-y>.
- Hürlimann, M., Rickenmann, D., Graf, C., 2003. Field and monitoring data of debris-flow events in the Swiss Alps. *Can. Geotech. J.* 40, 161–175. <https://doi.org/10.1139/t02-087>.
- Hürlimann, M., Coviello, V., Bel, C., Guo, X., Berti, M., Graf, C., Hübl, J., Miyata, S., Smith, J.B., Yin, H.-Y., 2019. Debris-flow monitoring and warning: Review and examples. *Earth Sci. Rev.* 199 <https://doi.org/10.1016/j.earscirev.2019.102981>.
- Jacquemart, M., Meier, L., Graf, C., Morsdorf, F., 2017. 3D dynamics of debris flows quantified at sub-second intervals from laser profiles. *Nat. Hazards* 89, 785–800. <https://doi.org/10.1007/s11069-017-2993-1>.
- Jakob, M., Hungr, O., 2005. *Debris-Flow Hazards and Related Phenomena*. Springer, Berlin, Heidelberg, New York.
- Lapillonne, S., Fontaine, F., Liebault, F., Richefeu, V., Piton, G., 2023. Debris-flow surges of a very active alpine torrent: a field database. *Nat. Hazards Earth Syst. Sci.* 23, 1241–1256. <https://doi.org/10.5194/nhess-23-1241-2023>.
- Li, J., Chen, N., Wang, T., Iqbal, J., Xiang, L., 2017. A model for total volume of debris flow with intermittent surges based on maximum peak discharge and movement time. *Geosyst. Eng.* 20, 181–194. <https://doi.org/10.1080/12269328.2016.1248298>.
- Lichtenhahn, C., 1971. Zwei Betonmauern: die Gieschieberückhaltesperre am Illgraben (VS) und die Staumauer des Hochwasserschutzbeckens an der Orlegna im Bergell (GR). In: Presented at the Int. Symposium Interpraevent 1971 des Oesterreichischen Wasserwirtschaftsverbandes, Villach, Kaernten, Austria, pp. 451–463.
- Liu, J., Li, Y., Su, P., Cheng, Z., Cui, P., 2009. Temporal variation of intermittent surges of debris flow. *J. Hydrol.* 365, 322–328. <https://doi.org/10.1016/j.jhydrol.2008.12.005>.
- Marchi, L., Cazorzi, F., Arattano, M., Cucchiaro, S., Cavalli, M., Crema, S., 2021. Debris flows recorded in the Moscardo catchment (Italian Alps) between 1990 and 2019. *Nat. Hazards Earth Syst. Sci.* 21, 87–97. <https://doi.org/10.5194/nhess-21-87-2021>.
- McArdell, B.W., 2016. Field measurements of forces in Debris Flows at the Illgraben: implications for Channel-Bed erosion. *Int. J. Eros. Control Eng.* 9, 194–198. <https://doi.org/10.13101/ijece.9.194>.
- McArdell, B.W., Sartori, M., 2021. The Illgraben Torrent System. In: Reynard, E. (Ed.), *Landscapes and Landforms of Switzerland*, World Geomorphological Landscapes. Springer International Publishing, Cham, pp. 367–378. https://doi.org/10.1007/978-3-030-43203-4_25.
- McArdell, B.W., Bartelt, P., Kowalski, J., 2007. Field observations of basal forces and fluid pore pressure in a debris flow. *Geophys. Res. Lett.* 34 <https://doi.org/10.1029/2006GL029183>.
- McArdell, B.W., Hirschberg, J., Graf, C., Boss, S., Badoux, A., 2023. Illgraben debris-flow characteristics 2019–2022. *EnviDat*. <https://doi.org/10.16904/enviDat.378>.
- Missbauer, P., 1971. Stützmauer für die Wildbachverbauung im Illgraben. Schweiz. Bauztg. 89, 1003–1006. <https://doi.org/10.5169/SEALS-85002>.
- Nagl, G., Hübl, J., Kaitna, R., 2020. Velocity profiles and basal stresses in natural debris flows. *Earth Surf. Process. Landf.* 45, 1764–1776. <https://doi.org/10.1002/esp.4844>.
- Ouster Inc, 2020. OS1 Mid-Range High resolution Imaging Lidar, Ouster OS-1 Gen1 data sheet [WWW Document]. OS1 -Range High Resolut. Imaging Lidar Ouster OS-1 Gen1 Data Sheet. URL. <https://data.ouster.io/downloads/datasheets/datasheet-gen1-v2p0-os1.pdf> (accessed 6.6.23).
- Rickenmann, D., 1999. Empirical Relationships for Debris Flows. *Nat. Hazards* 19, 47–77. <https://doi.org/10.1023/A:1008064220727>.
- Rickenmann, D., Zimmermann, M., 1993. The 1987 debris flows in Switzerland: documentation and analysis. *Geomorphology* 8, 175–189. [https://doi.org/10.1016/0169-555X\(93\)90036-2](https://doi.org/10.1016/0169-555X(93)90036-2).
- Rusu, R.B., Marton, Z.C., Blodow, N., Dolha, M., Beetz, M., 2008. Towards 3D Point cloud based object maps for household environments. *Robot. Auton. Syst. Semant. Knowled. Robot.* 56, 927–941. <https://doi.org/10.1016/j.robot.2008.08.005>.
- Spielmann, R., 2020. Analyzing Extremely Rapid, Flow-like Landslides Using Laser Scanning and Numerical Modeling (Bachelor's Thesis). ETH Zürich, Zurich.
- Spielmann, R., 2022. Understanding Debris-Flow Motion through Detailed Analysis of Timelapse Point Clouds Collected by High-Frequency 3D LiDAR Scanners; Illgraben, Switzerland (Master's Thesis). ETH Zürich, Zurich.
- Suwa, J.H., Okunishi, K., Sakai, M., 1993. Motion, debris size and scale of debris flows in a valley on Mount Yakedake, Japan. In: *Sediment Problems: Strategies for Monitoring, Prediction and Control*. Presented at the Yokohama Symposium, July 1993, IAHS press-intern ASSOC hydrological Scienc, Yokohama, p. 239.
- Theule, J.I., Crema, S., Marchi, L., Cavalli, M., Comiti, F., 2018. Exploiting LSPIV to assess debris-flow velocities in the field. *Nat. Hazards Earth Syst. Sci.* 18, 1–13. <https://doi.org/10.5194/nhess-18-1-2018>.
- Thielicke, W., Sonntag, R., 2021. Particle image velocimetry for MATLAB: accuracy and enhanced algorithms in PIVlab. *J. Open Res. Softw.* 9, 12. <https://doi.org/10.5334/jors.334>.
- Yan, Y., Cui, P., Guo, X., Ge, Y., 2016. Trace projection transformation: a new method for measurement of debris flow surface velocity fields. *Front. Earth Sci.* 10, 761–771. <https://doi.org/10.1007/s11707-015-0576-6>.